ACS APPLIED MATERIALS & INTERFACES

www.acsami.org

Research Article

Magnesium Ions Invert Selectivity and Electroosmotic Flow for Pristine Cation-Selective Nanopores

Domingo Francesco Iacoviello, Andrea Bonini, Simone Gargano, Peihong Zhai, Blasco Morozzo della Rocca, Giovanni Maglia, and Mauro Chinappi*

Cite This: https://doi.org/10.1021/acsami.6c06920

Read Online

ACCESS | Metrics & More | Article Recommendations | Supporting Information

ABSTRACT: Nanopore sensing has emerged as a powerful technique for single molecule detection, utilizing changes in ionic current to identify molecules as they interact with a nanopore. The applied voltage driving this process also induces an electroosmotic flow (EOF). EOF can be employed to capture different analytes independently of their charge and hence be used for protein sensing and sequencing. In this study, we investigate the impact of divalent cations on EOF for biological nanopores (MspA, CytK, and their mutants) using molecular dynamics (MD) simulations and experiments. Our results reveal that divalent cations induce a decrease in both ionic current and EOF magnitude with respect to K^+ in these cation-selective nanopores. This effect is caused by transient binding of divalent cations in the nanopore constriction, altering the effective surface charge of the nanopore and consequently modifying the cation/anion selectivity and the EOF.

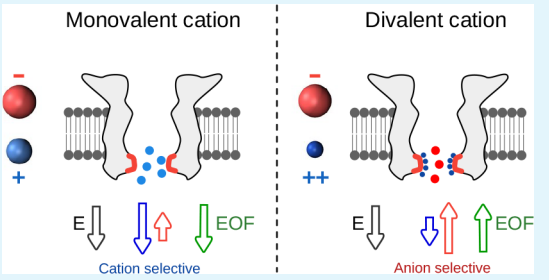

KEYWORDS: *electroosmosis, biological nanopores, MspA, CytK, $MgCl_2$, selectivity*

INTRODUCTION

Nanopore sensing is an established single-molecule technique that is largely employed in DNA sequencing.[1] Extending this approach to other molecules, such as proteins or sugars, is the goal of an intense applied research area.[2−9] One of the main challenges is controlling the capture and translocation of molecules in the pore. Indeed, capture rates control the throughput of the sensor, with low capture rates limiting the usefulness of the technology for the high-throughput needs of biochemical analysis, while translocation control is crucial to get stable and long signals and, consequently, it is fundamental to distinguish the different molecules. Capture and translocation are ruled by a complex interplay among different actions like electrophoresis, electroosmosis, and dielectrophoresis.[10] While for DNA the main driving force is electrophoresis, for neutral (or not homogeneously charged) classes of molecules like proteins, alternative mechanisms are needed to enforce capture and transport. In this respect, electroosmotic flow (EOF) has emerged as a powerful approach for nanopore sensing applications, as it can drive molecules independently of their charge.[11−17] Indeed, a general driving force such as EOF may also improve detection efficiency in complex systems and support the development of nanopore platforms toward single-molecule spatio-temporal omics.[18,19]

In the last decade, several strategies have been proposed to control EOF.[20] The most common method involves increasing the surface charge of the pore. Counterions accumulate close to the fixed surface charges, and the external electric field funneling into the pore acts on this accumulation, resulting in a force that drags the fluid. Hence, charge accumulation and ion mobility strongly affect the capability to transfer momentum toward the fluid. While monovalent cations have been extensively employed and studied in biological nanopore systems,[21−24] the impact of divalent cations such as Mg^{2+} remains less explored. Divalent metal ions have been used in MspA-based experiments involving engineered chelating or coordinating sites at the pore constriction.[25−27] Moreover, asymmetric $KCl/CaCl_2$ buffers have been shown to enhance and tune EOF in MspA-based nanopore sensing.[28,29] To date, only a few papers have addressed this phenomenon. Braha et al.[30] showed that engineered binding sites within a protein nanopore enable the detection of divalent cations, whose binding inside the pore produces measurable changes in the ionic current. Bhamidimarri et al.[31] reported that divalent ions alter pore selectivity and electroosmotic flow for the ΔCymA biological nanopore. However, a comprehensive description of how divalent ions modulate the electrohydrodynamics in cation-selective nanopores is still lacking. Understanding how divalent

Received: April 6, 2026
Revised: July 10, 2026
Accepted: July 10, 2026

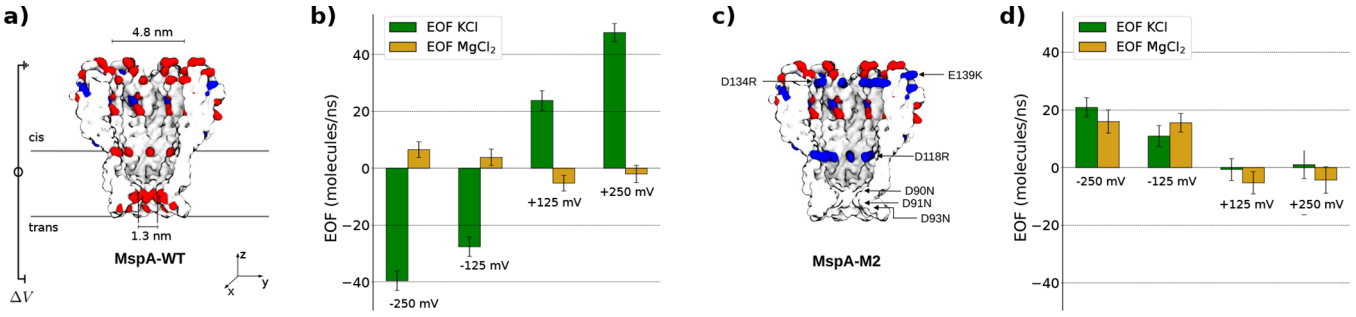

Figure 1. Electroosmotic flow (EOF) in MspA-WT and MspA-M2 in the presence of KCl and $MgCl_2$. (a, c) Longitudinal section of wild-type MspA and its M2 mutant. Positive and negative residues are represented in blue and red, respectively. The constriction region of MspA-WT is very negatively charged due to the presence of three aspartate residues at positions 90, 91, and 93. The MspA-M2 mutant features a neutral constriction (D90N, D91N, D93N) and additional mutations (D134R, E139K, D118R) that confer a slightly positive charge to the lumen. (b, d) EOF for the two pores at different applied voltages. In MspA-WT, for KCl, the EOF direction is consistent with expectations; for instance, at $\Delta V > 0$, EOF is positive, i.e., it has the same direction of the counterions. Conversely, for $MgCl_2$, in yellow, EOF decreases drastically and, under some conditions, reverses direction. Instead, for MspA-M2, the EOF is similar for both salts. Error bars represent the standard error of the mean obtained via block averaging over 120 ns for each voltage.

cations influence EOF in biological nanopores could provide valuable insights for optimizing nanopore-based technologies, especially for applications involving biomolecules that require specific ionic conditions.[32−35]

In this study, using all-atom molecular dynamics (MD) simulations, supported by single-channel electrophysiology, we investigate the electrohydrodynamic transport for divalent cation solutions flowing through several biological nanopores. We started with a $MgCl_2$ solution due to its relevance for nanopore sensing applications (in particular for nucleic acids, as Mg^{2+} is needed for the polymerase motor protein often used to control translocation[36−41]), and then, we extend our inquiry to Ca^{2+}, Zn^{2+}, and Mn^{2+}. The results on other divalent ions are, on the one hand, relevant from a biophysical perspective to show that the observed phenomena are robust and somehow generalizable, and, on the other hand, possibly useful for specific sensing applications, where Ca^{2+} is used,[29,42] and for future applications of biological membranes for cation separation (i.e., Mn is often present in lithium brines). We reveal that the accumulation of divalent cations at the pore walls results in an inversion of the ionic selectivity of the nanopore from cation- to anion-selective, with respect to control experiments with KCl. This inversion is often associated with the reversal of EOF. These findings highlight a possible non-invasive strategy to control electroosmotic flow: indeed, instead of modifying the pore internal charge via mutagenesis, the flow intensity and direction could be tuned by simply adjusting the electrolyte composition.

■ RESULTS AND DISCUSSION

Mg^{2+} Induces EOF and Selectivity Inversion for MspA

We measured, via MD simulations, the ionic current and electroosmotic flow in wild-type MspA (MspA-WT) and its mutant MspA-M2. MspA-WT features a cis opening of diameter 4.8 nm, while the constriction measures approximately 1.3 nm. The constriction region is highly negatively charged due to the presence of aspartate residues (D90, D91, D93), Figure 1a. In the MspA-M2 mutant, these negative charges are replaced by asparagine (D90N, D91N, D93N),[43] neutralizing the overall charge of the constriction, Figure 1c. We first studied the ion and water transport in two electrolyte solutions: 1 M KCl and 0.33 M $MgCl_2$. The choice of a lower concentration for $MgCl_2$ was made to maintain the same ionic strength $I_s = \frac{1}{2}\sum_i c_i z_i^2$, where the summation is on the ionic species, c_i is the ionic concentration of the i-th species, and z_i is its valence. This choice was used as a nominal guideline to keep the ionic strength, and hence the continuum Debye length, comparable in the two electrolytes. In this sense, 1 M KCl and 0.33 M $MgCl_2$ allow us to compare systems with similar nominal electrostatic screening (at the continuum level) while focusing on ion-specific effects beyond a simple continuum description.

Electroosmotic Flow. In MspA-WT with 1 M KCl, we observe a strong EOF directed from the cis to the trans side at negative voltages, Figure 1b. EOF follows the direction of the applied electric field, as expected for cation-selective nanopores.[12,14,16,44] In contrast, in 0.33 M $MgCl_2$, MspA-WT shows a marked reduction in EOF magnitude, with an inversion of the EOF direction, so that now, for $\Delta V < 0$, the flow is directed from trans to cis. For comparison, in MspA-M2, where the constriction charge is neutralized, there is no significant difference in EOF between KCl and $MgCl_2$, Figure 1d. For both salts, the EOF direction for $\Delta V < 0$ is from trans to cis, in line with the mild prevalence of exposed positive residues in the MspA-M2 lumen. As expected, the EOF magnitude is reduced compared to MspA-WT with KCl, as surface charges are known to be most effective in modulating EOF when located within the constriction.[14]

Ionic Current and Selectivity. The EOF measurements reported in Figure 1 show that the presence of divalent cations in negatively charged pores results in both the reduction and the inversion of EOF. To gain more insights, we analyzed the ionic currents. For MspA-WT, the total ionic current in 0.33 M $MgCl_2$ is smaller than that in 1 M KCl, Figure 2a,c. While the current in the KCl system is dominated by the cation contribution, the cation current in the $MgCl_2$ system is negligible; essentially no net transport of Mg^{2+} is observed in MspA-WT. The presence of Mg^{2+} inverts the pore selectivity from the expected cation selectivity (due to the negative charges exposed in the constriction of MspA-WT) to anion selectivity. This inversion aligns with the EOF reversal shown in Figure 1. Furthermore, although 0.33 M $MgCl_2$ and 1 M KCl have the

https://doi.org/10.1021/acsami.6c06920
ACS Appl. Mater. Interfaces XXXX, XXX, XXX−XXX

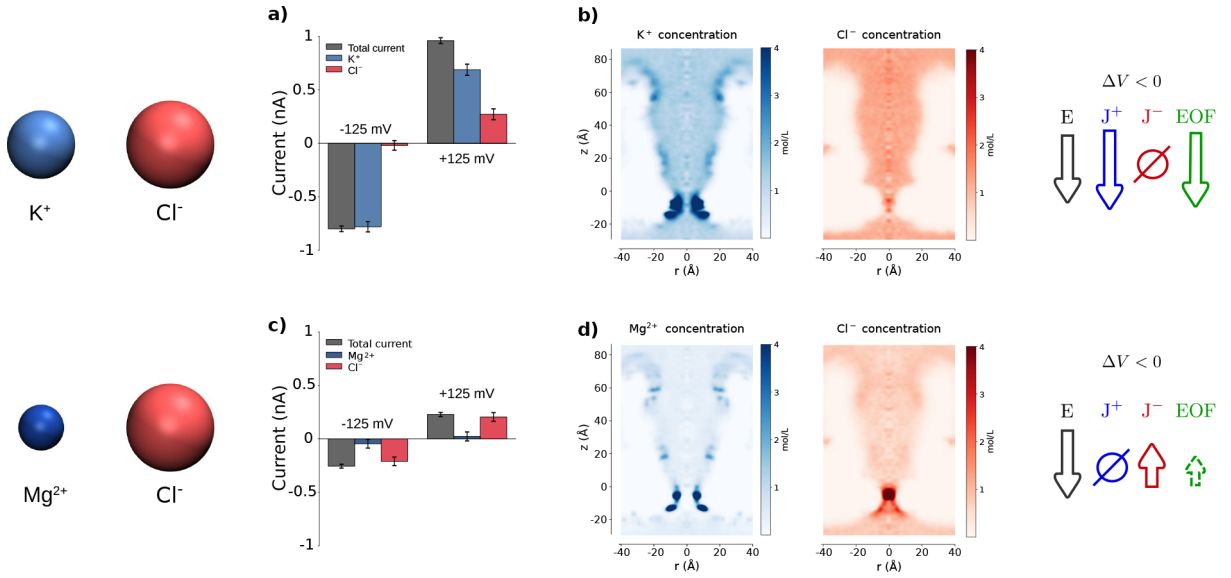

Figure 2. Ionic currents and charge distribution in MspA-WT for 1 M KCl and 0.33 M $MgCl_2$. Total, cationic, and anionic currents in the presence of 1 M KCl (a) and 0.33 M $MgCl_2$ (c). For $MgCl_2$, the cationic current is negligible, while the anionic contribution dominates the total current. Error bars represent the standard error of the mean obtained via block averaging over 120 ns for each voltage. (b, d) Charge density maps at equilibrium, $\Delta V = 0$, showing the distribution of cations (blue) and anions (red) within the lumen of MspA-WT. Despite the two electrolyte solutions having the same λ_D, as calculated from the Poisson–Nernst–Planck theoretical model, Note S1, the accumulation of cations in the negatively charged constriction differs between the two salts, with much thinner cation clouds for Mg^{2+} than for K^+. For $MgCl_2$, an accumulation of anions is also observed in the constriction.

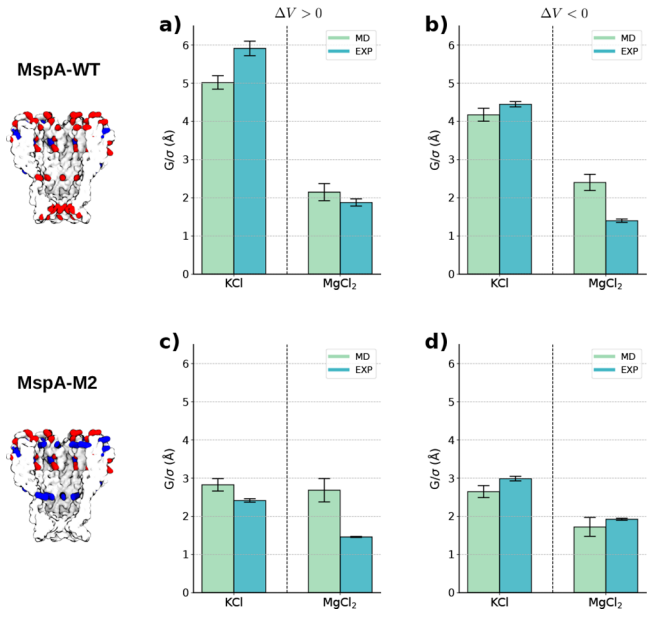

Figure 3. Normalized nanopore conductance. Bars represent MD and electrophysiological measurements for the conductance G of the pore divided by the conductivity (σ) of the electrolyte solution. Experimental data refer to $\Delta V = \pm 100$ mV, and MD simulations refer to $\Delta V = \pm 125$ mV (same dataset of Figures 1 and 2). Data are shown for MspA-WT (a, b) and MspA-M2 (c, d), with positive (left) and negative (right) applied voltages. A strong reduction of conductance is observed for divalent ions in MspA-WT. Experimental I–V curves are reported in Figure S3.

same Debye length (λ_D), a qualitative difference in the cation distribution within the constriction is evident, Figure 2b,d. In the KCl system, cations accumulate within the negatively charged constriction of MspA-WT, reducing the available space for anions. For $MgCl_2$, cations also accumulate in the constriction; however, they form a thinner cloud compared to KCl, and an accumulation of Cl^- can be observed. In essence, with $MgCl_2$, MspA-WT acts as an anion-selective pore with a strong accumulation of anions in its constriction, resulting in anion selectivity and an EOF directed accordingly. For comparison, the results for MspA-M2 are reported in Figure S1, showing no inversion of EOF as the constriction is neutral. The overall conclusions are also confirmed by simulations carried out with different force fields,[45,46] see Figure S2.

Electrophysiology experiments were conducted to support the MD simulation results. EOF cannot be directly measured from experiments,[47] and, moreover, a quantitative agreement is not expected even for ionic currents, as discrepancies in the conductivity of the electrolyte solution are present.[22,45,48] Consequently, our experimental approach is aimed at validating the strong reduction of ionic current for $MgCl_2$. We experimentally measured the pore conductance $G = I/\Delta V$ for both pore mutants and both salts at $\Delta V = \pm 100$ mV. To decouple the pore transport properties from the bulk solution conductivity σ, we analyzed the normalized conductance G/σ, Figure 3. For MspA-WT (Figure 3a,b), a drastic reduction in G/σ is observed when switching from KCl to $MgCl_2$, at both positive and negative voltages. This drop indicates that the pore conductivity decreases disproportionately with respect to the bulk conductivity. This finding corroborates the picture emerging from

https://doi.org/10.1021/acsami.6c06920
ACS Appl. Mater. Interfaces XXXX, XXX, XXX–XXX

MD simulations: the divalent cations are trapped at the negatively charged constriction, strongly reducing the portion of the pore available for the passage of the electrolyte solution. Conversely, this effect is mitigated in the MspA-M2 mutant (Figure 3c,d), confirming that the strong blocking effect is driven by the constriction charge. This is also confirmed by control simulations for the MspA-M2-R118D nanopores, where the negative charge is placed not in the constriction but in a wider section, see Figure S5.

Mixed Salt Solution. To investigate whether the EOF and selectivity inversion due to Mg^{2+} persist in the presence of competing monovalent cations, we conducted simulations with a mixed solution containing 0.25 M KCl and 0.25 M $MgCl_2$, maintaining a total ionic strength of $I_s = 1$ M. EOF in this mixed solution was similar both in magnitude and direction to the 0.33 M $MgCl_2$ one, Figure 4a. Analysis of individual ionic currents revealed a voltage-dependent asymmetry. At −125 mV, K^+ current was minimal, while Mg^{2+} and Cl^- currents were higher. At +125 mV, both cation currents were reduced, whereas Cl^- current increased substantially, Figure 4b. The equilibrium charge density maps in the mixed salt solution display a very similar profile to the one observed for 0.33 M $MgCl_2$, with both Mg^{2+} and Cl^- accumulating in the constriction region of MspA-WT, see Figure 4c. In contrast, K^+ remains almost uniformly distributed along the pore, resulting in asymmetric distribution of the different cation species. Taken together, these results indicate that Mg^{2+} preferentially binds the negative constriction with respect to K^+ and, consequently, suggest that the EOF and the selectivity of a pristine cation-selective nanopore are mainly dominated by the divalent ions. We also preliminarily explored the role of divalent ion concentrations in the mixed salt solution. The data show that decreasing the concentration of divalent salt (while keeping the KCl concentration constant) smoothed the selectivity and EOF modulation, see Figure S6.

Mg^{2+} Binds the MspA-WT Constriction

A possible interpretation of the data reported up to now is that Mg^{2+} ions, by virtue of their higher charge, may bind more stably to the constriction of MspA-WT, where three rings of aspartic acids are present. This binding would, de facto, invert the effective surface charge and, consequently, result in an inversion of the system's cation/anion selectivity. This explanation aligns with previous findings reported for the ΔCymA pore.[31] Furthermore, the cation density maps in Figure 2 indicate that the localized accumulation of Mg^{2+} is more pronounced than that of K^+. This is in contrast with what is expected from ideal electrokinetic theories. Indeed, given that both solutions maintain the same ionic strength, the Debye length remains constant; hence, the ionic clouds should exhibit the same spatial extent. However, Figure 2 shows a more sharply peaked accumulation of Mg^{2+}, suggesting a deviation from the ideal behavior.

To assess this effect quantitatively, we evaluated the ion residence time within the constriction region. The representative trajectories for Mg^{2+} (Figure 5a) and K^+ (Figure 5b) show a longer occupancy of Mg^{2+} compared with the brief transit of K^+. The average residence times within the constriction are significantly higher for Mg^{2+} across all applied voltages, confirming a stronger interaction of Mg^{2+} with the negative surface charges, Figure 5c.

Ionic Currents and EOF for CytK Mutants

We extended the analysis to the CytK-2E4D mutant nanopore.[16] The simulations confirm the scenario that emerged from the analysis of MspA. As expected, a pore exposing negative charges in the lumen is highly selective for cations in 1 M KCl, Figure 6a. The equilibrium charge density map clearly illustrates the accumulation of K^+ cations along the negatively charged walls of the pore, Figure 6b. However, in the presence of 0.33 M $MgCl_2$, the total ionic current is strongly reduced and the pore exhibits slight anion selectivity, Figure 6d. This shift is driven by the strong interaction of divalent Mg^{2+} ions with the negative lumen. In essence, this behavior mirrors the mechanism observed in MspA, but the spatial distribution of the ions differs due to pore geometry. While MspA features a short and narrower constriction where Cl^- accumulates throughout the entire constriction, CytK-2E4D possesses an elongated, negatively charged β-barrel. In CytK-2E4D, the Cl^- accumulation is distributed along the barrel with a peak in its lower portion, where a double ring of negative residues (D128, E139) induces a more intense accumulation of Mg^{2+}, Figure 6e. As a result of this localized accumulation and the partial adhesion of Mg^{2+}, the overall ionic currents are strongly diminished. This directly translates to a reduced EOF compared to the KCl case

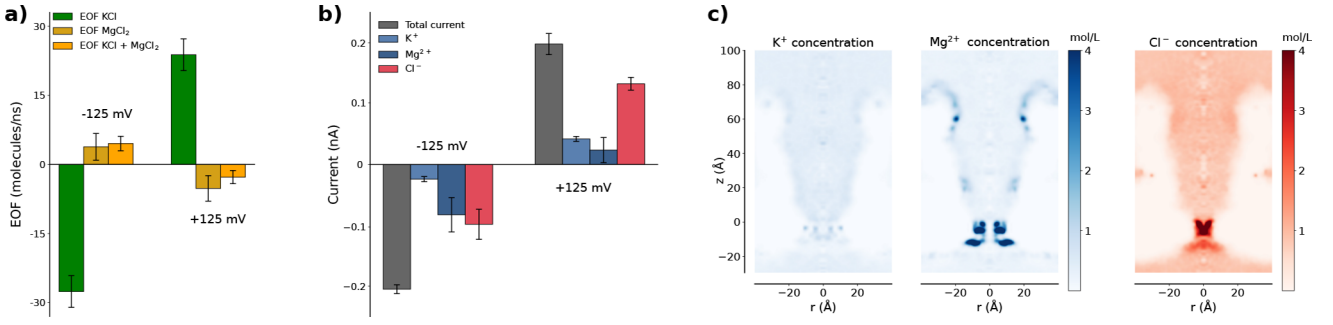

Figure 4. Electroosmotic flow and ionic current in mixed salt solutions. (a) EOF measured in three ionic conditions: 1 M KCl, 0.33 M $MgCl_2$, and a mixed salt solution (0.25 M KCl + 0.25 M $MgCl_2$), at applied voltages of ±125 mV. The EOF in the mixed salt solution exhibits behavior similar to that observed in 0.33 M $MgCl_2$, distinct from the 1 M KCl condition. (b) Total ionic current and individual species contributions (K^+, Mg^{2+}, and Cl^-) in the mixed salt solution at ±125 mV. At −125 mV, K^+ current is minimal, while Mg^{2+} and Cl^- currents are higher, with Cl^- current slightly exceeding that of Mg^{2+}. At +125 mV, K^+ and Mg^{2+} currents are both reduced, while Cl^- current is substantially elevated. (c) Equilibrium charge density distributions for K^+, Mg^{2+}, and Cl^- in MspA. Mg^{2+} and Cl^- show strong accumulation in the constriction region, whereas K^+ remains uniformly distributed. Error bars represent the standard error of the mean calculated via block averaging.

https://doi.org/10.1021/acsami.6c06920
ACS Appl. Mater. Interfaces XXXX, XXX, XXX−XXX

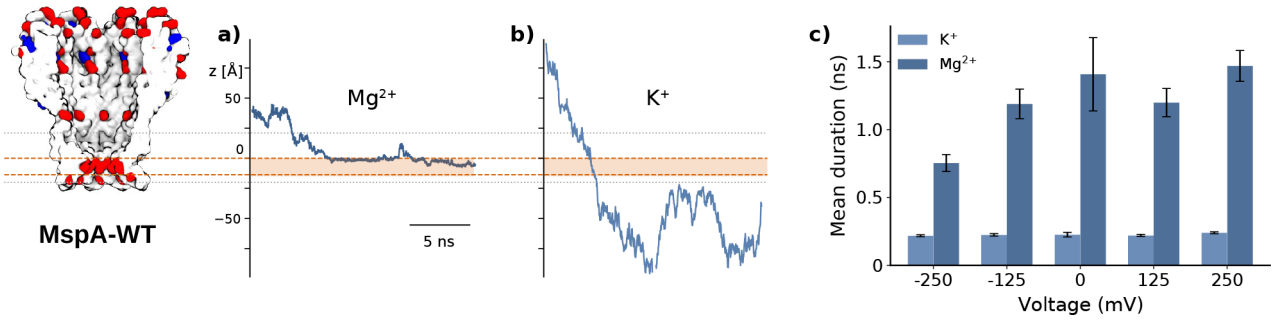

Figure 5. Residence time of Mg^{2+} and K^+ in the constriction. (a) Representative time evolution of the z coordinate of a Mg^{2+} ion in MspA-WT. The orange shaded region marks the pore constriction, aligned with the structural model on the left, where aspartic acid residues are exposed. The ion is transiently trapped in this region. (b) Representative trajectory for a K^+ ion, which translocates through the constriction without observable trapping events. (c) Mean residence duration of K^+ and Mg^{2+} within the constriction as a function of applied voltage (corresponding ion counts are reported in Figure S9). In contrast to the rapid translocation of K^+, Mg^{2+} ions show longer residence times. Error bars represent the standard error of the mean.

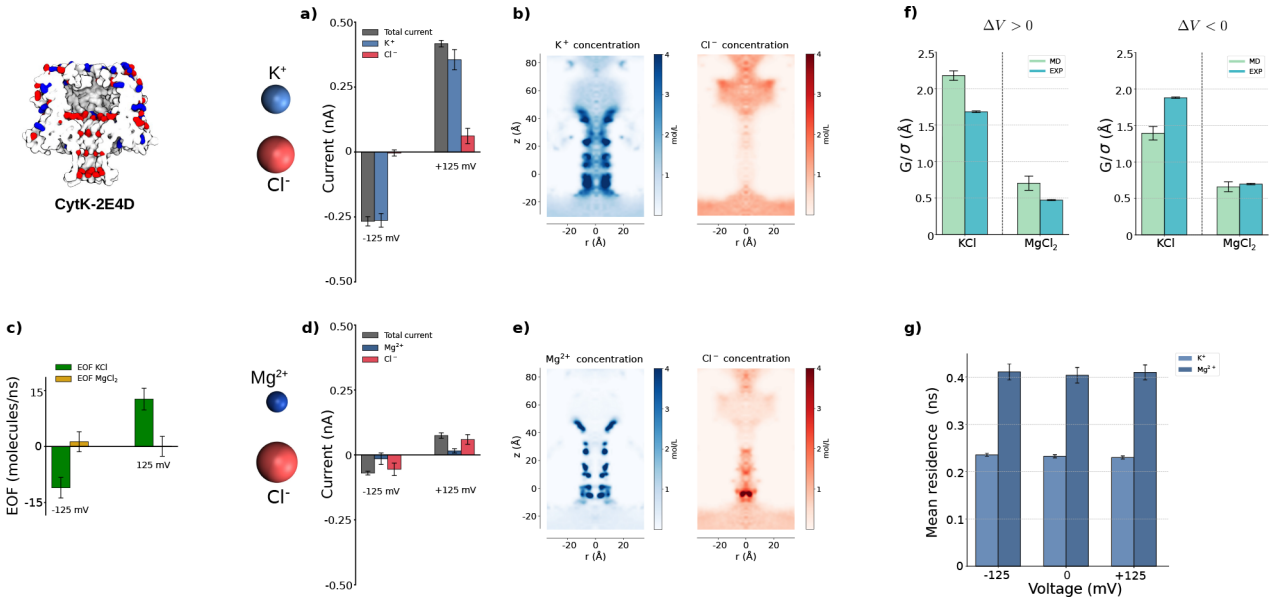

Figure 6. Ionic currents, EOF, and charge distribution in CytK-2E4D for 1 M KCl and 0.33 M $MgCl_2$. Total, cationic, and anionic currents in the presence of 1 M KCl (a) and 0.33 M $MgCl_2$ (d). Error bars represent the standard error of the mean obtained via block averaging. (b, e) Charge density maps at equilibrium, $\Delta V = 0$, showing the distribution of cations (blue) and anions (red) within the lumen of CytK-2E4D. (c) EOF. (f) Bars represent MD and electrophysiological (EXP) measurements for the conductance G of the CytK-2E4D pore divided by the conductivity σ of the electrolyte solution (see Figure S3 for experimental I–V curves). (g) Mean residence duration of K^+ and Mg^{2+} within the constriction as a function of applied voltage. In contrast to the rapid translocation of K^+, Mg^{2+} ions show longer residence times. Error bars represent the standard error of the mean.

(Figure 6c) and a reduction of conductance, yielding results in agreement with experimental electrophysiological measurements, Figure 6f. This strong adhesion is further confirmed by the extended residence times of Mg^{2+} within the constriction, Figure 6g. The MD findings are corroborated experimentally by reversal potential measurements showing that, despite CytK-2E4D having fixed negative charges, with $MgCl_2$, the system is anion-selective, see Figure S4. As a further test, we explored the effect of the number of charges in the CytK β-barrel using MD simulations of a simplified system in which the vestibule is not modeled. The results indicate that the presence of only a single or a double ring of fixed negative charges yields no effect on selectivity and EOF, Figure S7.

Other Divalent Ions

As a final test, we explored other divalent ions to understand whether the results were limited to the specific properties of Mg^{2+}, or if the reduction/inversion of the selectivity and EOF is a general effect of divalent cations in pores exposing negative charges. Results for Ca^{2+}, Zn^{2+}, and Mn^{2+} are reported in Figure 7. The overall behavior is confirmed. Specifically, for MspA, an inversion of selectivity and EOF is consistently observed across the different salts. For CytK-2E4D, as with Mg^{2+}, the currents are very low, especially in the case of Ca^{2+}, whose charge density maps show a different accumulation pattern. These findings indicate that for other divalent ions as well, the large negative surface charge of the pore barrel binds

https://doi.org/10.1021/acsami.6c06920
ACS Appl. Mater. Interfaces XXXX, XXX, XXX–XXX

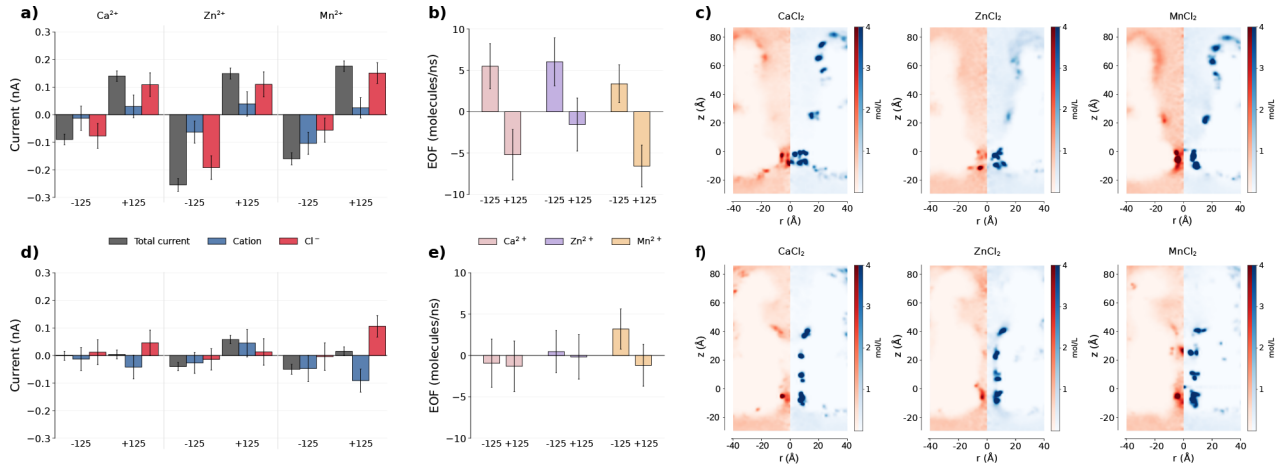

Figure 7. EOF and selectivity for other divalent ions. (a) Total, cationic, and anionic currents for MspA for 0.33 M solution of $CaCl_2$, $ZnCl_2$, and $MnCl_2$. Error bars represent the standard error of the mean obtained via block averaging. The corresponding EOF is in panel (b) while the charge density maps at equilibrium, $\Delta V = 0$, are in panel (c). (d–f) Same data for CytK.

the divalent ions strongly enough to reduce the mobility of both ions and water, see Figure S8.

■ CONCLUSIONS

Molecular dynamics simulations and single-channel electrophysiology demonstrate that the presence of divalent cations fundamentally alters the electrohydrodynamic transport in biological nanopores featuring negatively charged constrictions (MspA-WT and CytK-2E4D). Compared to monovalent ions, divalent cations induce a severe reduction in overall ionic conductance and EOF magnitude. Furthermore, divalent cations invert both the ionic selectivity from cation- to anion-selective and the direction of the EOF. Analysis of ion dynamics reveals that this inversion is driven by the extended residence time of divalent cations within the negatively charged constriction zones. This strong transient binding alters the effective surface charge of the lumen, locally creating an anion-selective environment and promoting Cl^- accumulation, which, in some cases, may result in an inversion of the EOF direction. This mechanism is validated by the absence of EOF inversion in the control simulation with the charge-neutralized mutant (MspA-M2) and by the dominant effect of Mg^{2+} observed under mixed-salt conditions. Experimental conductance measurements corroborate the computational data, confirming a disproportionate current drop, likely driven by the electrostatic interaction at the constriction. Testing different cations yielded the same overall behavior. These findings suggest that the EOF intensity and direction can be modulated by adjusting the electrolyte valency and composition, providing a practical alternative to the targeted mutagenesis of the nanopore lumen. Consequently, tuning the electrolyte formulation offers a variable to control electrohydrodynamic transport, which could prove useful for influencing the capture and translocation of biomolecules in nanopore experiments.

■ METHODS

General MD Methods

All MD simulations were performed using NAMD 2.14.[49] The methods are similar to those reported in ref 50, which were inspired by Aksimentiev et al.[22] The CHARMM36[51] force field with CUFIX corrections,[52] periodic boundary conditions, and the particle mesh Ewald (PME) method with a 1.0 Å spaced grid for long-range electrostatic interactions were employed.[53] van der Waals energies were calculated using a 12 Å cutoff with a switching distance of 10 Å. The integration timestep was 1 fs in equilibration runs and 2 fs in all non-equilibrium simulations. A Langevin thermostat was used for all the simulations, while a Nosè–Hoover Langevin piston pressure control was used for constant pressure equilibrations (NPT ensemble).[54] The scaling parameter was set to 1.0 for CHARMM36-based simulations and 0.833333 for Amber-based[55] simulations.

MD System Setup

Atomic coordinates of MspA were taken from an X-ray crystal structure in the Protein Data Bank, PDB_ID: 1UUN[56] downloaded from the OPM database.[57] Arginine 96 was mutated to alanine in order to restore the WT sequence. This structure was oriented to align the symmetry axis of the protein with the z axis. A POPC bilayer was generated with the VMD[58] plugin Membrane Builder and was oriented parallel to the x–y plane. The protein was embedded into the membrane and lipids overlapping with the pore or located inside the channel were removed. The protein–membrane complex was solvated in a TIP3P water box (140 Å × 140 Å × 190 Å) in which ions were added depending on the system conditions simulated. The final system contains ∼333k atoms. The MspA mutants, M2 and M2-R118D, were obtained starting from the wild-type structure. Point mutations were performed using VMD Mutate plugin on each MspA chain recursively. The CytK-2E4D structure was taken from Sauciuc et al.[16] For Amber-ff14SB[59] and Amber-ff19SB[60] simulations (with TIP3P[61] and OPC[62] water, respectively), additional steps were necessary to produce a prmtop file and to convert the CHARMM36-formatted pdb file into an Amber-formatted pdb file (see ref 45). For the Mn^{2+} force field, we employed the parameters included in the CHARMM supplemental datasets.[63]

Equilibration

The whole process that will be described is valid for all the systems simulated. The energy of the system was initially

https://doi.org/10.1021/acsami.6c06920
ACS Appl. Mater. Interfaces XXXX, XXX, XXX–XXX

minimized for 5000 steps. The system was equilibrated in 3 steps with a constant pressure run (NPT) at $P = 1$ atm and $T = 300$ K. A first equilibration of 600 ps was performed to let the lipid tails and the electrolyte to relax. The temperature was increased from 0 to 300 K in 130 ps, and the ratio between the x and y axes was kept constant. External forces were applied to keep the water molecules out of the membrane, while the C_α values were fixed and lipid heads were constrained with harmonic springs $K_b = 1$ kcal/(mol Å^2) only along the z axis. A second equilibration run of 500 ps was performed, where the C_α values were fixed and the lipid heads were harmonically constrained only to their x–y position with the same spring constant. The last equilibration step consisted of a 2 ns run, where all atoms were unconstrained and no external force was applied. At the end of the equilibration, the dimensions of the box were 126–128 Å × 126–128 Å × 204–197 Å (since independent equilibration was run for the different systems, the final size of the box may slightly change).

Ionic Currents from MD

The non-equilibrium runs were performed at constant particle number, volume, and temperature (NVT). All simulations were conducted for 40 ns. For each sample, a uniform and constant external electric field $E = (0, 0, E_z)$ was applied perpendicularly to the membrane. A total of 5 different voltages were applied: 0, ±0.125, and ±0.25 V. The average ionic current in the interval $[t, t + \Delta t]$ was computed as follows:

$$I(t) = \frac{1}{\Delta t L_z} \sum_{i=1}^{N} q_i [z_i(t + \Delta t) - z_i(t)] \quad (1)$$

where q_i and z_i are the charge and the z-coordinate of atom i, respectively. Ionic currents were computed by restricting the sum to the atoms of the corresponding type. The mean current is obtained with a block average of $I(t)$, where each block corresponds to 1.66 ns, after discarding the first 10 ns of the simulation. The EOF is measured in a similar way, computing the summation over the fluid atoms and using the mass instead of the charge in eq 1.

Ion and Water Density Fields from MD

Following a procedure presented in previous works[14,21,50] of our group, the box was initially divided into cubic cells with a side length of 1 Å. The average density for water, cations, and anions in each cell was calculated using the "Volmap" plug-in of VMD.[58] The 3D density fields were then transformed from the Cartesian coordinate system to a cylindrical coordinate system with respect to the nanopore axis. Finally, averaging over the angular coordinates allowed us to get the (r, z) maps represented in the manuscript.

Estimation of the Residence Time from MD

Analyses were performed on 30 ns production trajectories, with atomic coordinates sampled every 20 ps. A region of interest (RoI) was defined along the principal symmetry axis (z-axis) to encompass the constriction zones and primary binding sites. The RoI boundaries were set from $z = 5$ Å to $z = -15$ Å for the MspA pore and from $z = 35$ Å to $z = -15$ Å for the CytK-2E4D pore. A residence event was defined as a continuous sequence of simulation frames during which an ion's z-coordinate remained within the RoI. Multiple transits by the same ion, characterized by exiting and subsequently re-entering the region, were treated as independent events. The duration of each event was calculated as the time elapsed between the ion's entry into and exit from the RoI.

Experimental Measurements

Chemicals: DPhPC was purchased from Avanti Polar Lipids. n-Hexadecane (99%) was purchased from Acros Organics. Pentane (99%) was purchased from ThermoFisher Scientific. Potassium chloride, Tris-HCl, and magnesium chloride were purchased from Roth.

Protein Expression and Purification

The nanopores were expressed and purified according to established published protocols for MspA-WT,[64] MspA-M2,[14] and CytK-2E4D.[16] The sequences of the nanopores used in this study are as follows:

MspA-WT:

MGLDNELSLVDGQDRTLTVQQWDTFLNGVFPLDRN
RLTREWFHSGRAKYIVAGPGADEFEGTLELGYQIGFPWS
LGVGINFSYTTPNILIDDGDITAPPFGLNSVITPNLFPGVS
ISADLGNGPGIQEVATFSVDVSGAEGGVAVSNAHGTVTG
AAGGVLLRPFARLIASTGDSVTTYGEPWNMNGSAGSAW
SHPQFEK

MspA-M2:

MGLDNELSLVDGQDRTLTVQQWDTFLNGVFPLDRN
RLTREWFHSGRAKYIVAGPGADEFEGTLELGYQIGFPWS
LGVGINFSYTTPNILINNGNITAPPFGLNSVITPNLFPGVS
ISARLGNGPGIQEVATFSVRVSGAKGGVAVSNAHGTVTG
AAGGVLLRPFARLIASTGDSVTTYGEPWNMNGSAGSAW
SHPQFEK

CytK-2E4D:

MAQTTSQVVTDIGQNAKTHTSYNTFNNEQADNMT
MSLKVTFIDDPSADKQIAVINTTGSFMKANPTLSDAPVD
GYPIPGASVTLRYPSQYDIAMNLQDNTSRFFHVAPTNAV
EETTVTSSVSYQLGGSIDASVTPSGPSGESGATGDVTWSD
DVSYDQTSYKTNLIDQTNKHVKWNVFFNGYNNQNWG
IYTRDSYHALYGNQLFMYSRTYPHETDARGNLVPMNDL
PTLTNSGFSPGMIAVVISEKDTEQSSIQVAYTKHADDYTL
RPGFTFGTGNWVGNNIKDVDQKTFNKSFVLDWKNKKL
VEKKGSAHHHHHH

Single-Channel Recording Experiments

Single-channel measurements in a planar lipid bilayer setup were performed using a custom-designed chamber consisting of two compartments separated by a 25 μm thick Teflon membrane with an aperture of approximately 100 μm, as previously described by Maglia et al.[65] A droplet of n-hexadecane dissolved in n-pentane (4% v/v) was applied to the Teflon membrane. Subsequently, 450 μL of buffer solution was added to each compartment, followed by the addition of two droplets of DPhPC solution (5 mg/mL in n-pentane). Ag/AgCl electrodes were then connected to each compartment, with the cis compartment grounded.[66] After the formation of the lipid bilayer, a nanopore solution was added, and a single nanopore was isolated. Measurements were performed using an Axopatch 200B amplifier and an Axon Digidata 1550B digitizer (Molecular Devices), with data acquired using Clampex 11.1 software. Current–voltage (I–V) curves were recorded over a voltage range from −100 to +100 mV in 5 mV increments (sampling rate: 10 kHz; low-pass filtered at 2 kHz using a Bessel filter).

https://doi.org/10.1021/acsami.6c06920
ACS Appl. Mater. Interfaces XXXX, XXX, XXX–XXX

Buffers used: (i) 1 M KCl, 10 mM Tris-HCl, pH 7.4 (ii) 0.33 M $MgCl_2$, 10 mM Tris-HCl, pH 7.4.

Reversal Potential Experiments

Single-nanopore recordings were performed under symmetric electrolyte conditions using a buffer containing 2 M $MgCl_2$ and 10 mM Tris-HCl, pH 7.0. After isolation of a single nanopore, the pipette offset was adjusted to 0 pA at 0 mV applied bias. Current–voltage curves were obtained by recording the ionic current between −100 and +100 mV in 5 mV increments using a sampling rate of 10 kHz and a 2 kHz Bessel filter.

The $MgCl_2$ concentration in the *trans* compartment was then reduced to 0.5 M by perfusion with a buffer containing 0.5 M $MgCl_2$ and 10 mM Tris-HCl, pH 7.0. A second current–voltage curve was recorded under asymmetric electrolyte conditions using the same acquisition protocol.

The reversal potential was determined from this second current–voltage curve. For each condition, current–voltage measurements were performed in triplicate. The current values recorded between −100 and +100 mV were fitted by linear regression using Excel, and the voltage corresponding to zero current was calculated from the fitted equation. This voltage was defined as the reversal potential, V_r, and used to solve the Goldman–Hodgkin–Katz (GHK) equation modified for divalent ions, see Note S2.

■ ASSOCIATED CONTENT

Supporting Information

The Supporting Information is available free of charge at https://pubs.acs.org/doi/10.1021/acsami.6c06920.

Ionic strength and Debye length, GHK selectivities data for ionic currents and charge map for MspA-M2, current and EOF force field comparison for MspA nanopores, experimental IV curves, reversal potential, MD data for charge mutants and mixed salts, additional experimental data for $CaCl_2$, and mean ion count in MspA-WT constriction (PDF)

■ AUTHOR INFORMATION

Corresponding Author

Mauro Chinappi – *Department of Industrial Engineering, University of Rome Tor Vergata, Via del Politecnico 1, 00133 Rome, Italy*; orcid.org/0000-0002-4509-1247; Email: mauro.chinappi@uniroma2.it

Authors

Domingo Francesco Iacoviello – *Department of Industrial Engineering, University of Rome Tor Vergata, Via del Politecnico 1, 00133 Rome, Italy*

Andrea Bonini – *Department of Chemistry "Ugo Schiff", University of Florence, Via della Lastruccia 3, Sesto Fiorentino, FI 50019, Italy*

Simone Gargano – *Department of Industrial Engineering, University of Rome Tor Vergata, Via del Politecnico 1, 00133 Rome, Italy*

Peihong Zhai – *Groningen Biomolecular Sciences and Biotechnology Institute, University of Groningen, Groningen 9747 AG, The Netherlands*

Blasco Morozzo della Rocca – *Department of Biology, University of Rome Tor Vergata, Via della Ricerca Scientifica 1, 00133 Rome, Italy*; orcid.org/0000-0001-5491-1131

Giovanni Maglia – *Groningen Biomolecular Sciences and Biotechnology Institute, University of Groningen, Groningen 9747 AG, The Netherlands*; orcid.org/0000-0003-2784-0811

Complete contact information is available at: https://pubs.acs.org/doi/10.1021/acsami.6c06920

Notes

The authors declare the following competing financial interest(s): The other authors declare no conflict of interest. G.M. is the founder, director, and shareholder in Portal Biotech Limited, a nanopore engineering company. This work was not supported by Portal Biotech Limited.

■ ACKNOWLEDGMENTS

MspA simulations were run using HPC computational resources provided by the Swiss National Supercomputing Centre (CSCS), project ID s1280. CytK and mixed solution simulations were run on CINECA LEONARDO, project IsB29 ENATOPS2. The PhD scholarships for D.F.I. and S.G. were supported by PNRR (Piano Nazionale di Ripresa e Resilienza), funded by the European Union (Next Generation EU). We thank Marco Reccia for providing the MD setup for the CytK-barrel simulations.

■ REFERENCES

(1) Jain, M.; Fiddes, I. T.; Miga, K. H.; Olsen, H. E.; Paten, B.; Akeson, M. Improved data analysis for the MinION nanopore sequencer. *Nat. Methods* **2015**, *12*, 351.

(2) Mereuta, L.; Roy, M.; Asandei, A.; Lee, J. K.; Park, Y.; Andricioaei, I.; Luchian, T. Slowing down single-molecule trafficking through a protein nanopore reveals intermediates for peptide translocation. *Sci. Rep.* **2014**, *4*, 3885.

(3) Ratinho, L.; Bacri, L.; Thiebot, B.; Cressiot, B.; Pelta, J. Identification and detection of a peptide biomarker and its enantiomer by nanopore. *ACS Central Sci.* **2024**, *10*, 1167–1178.

(4) Wang, K.; Yang, X.; Zhang, S.; Zhang, P.; Huang, S. Nanopore discrimination of nucleotide sugars. *Nano Lett.* **2023**, *23*, 8620–8627.

(5) Sk, S.; Majumdar, B. B.; Vikraman, D.; Mahanta, K.; Soman, A.; Rajavelu, A.; Mondal, J.; Mahendran, K. R. A Dynamic Sugar-Selective Bacterial Nanopore for Targeted Antibiotic Transport. *Small* **2025**, *21*, 2502110.

(6) Bonini, A.; Lu, C.; Mantovanelli, L.; Versloot, R. C. A.; Jansen, A.; O'Connell Stack, P.; Tsousi, V.; Knecht, P.; Lang, K.; Heron, A., et al. Single-molecule identification of full-length proteins with single-amino-acid resolution using nanopores. *bioRxiv* **2026**.

(7) Straathof, S.; Di Muccio, G.; Maglia, G. Nanopores with an Engineered Selective Entropic Gate Detect Proteins at Nanomolar Concentration in Complex Biological Sample. *J. Am. Chem. Soc.* **2025**, *147*, 15050–15065.

(8) Willems, K.; Ruic, D.; Biesemans, A.; Galenkamp, N. S.; Van Dorpe, P.; Maglia, G. Engineering and modeling the electrophoretic trapping of a single protein inside a nanopore. *ACS Nano* **2019**, *13*, 9980–9992.

(9) Lu, C.; Bonini, A.; Viel, J. H.; Maglia, G. Toward single-molecule protein sequencing using nanopores. *Nat. Biotechnol.* **2025**, *43*, 312–322.

(10) Chinappi, M.; Yamaji, M.; Kawano, R.; Cecconi, F. Analytical model for particle capture in nanopores elucidates competition among

electrophoresis, electroosmosis, and dielectrophoresis. *ACS Nano* **2020**, *14*, 15816–15828.
(11) Asandei, A.; Schiopu, I.; Chinappi, M.; Seo, C. H.; Park, Y.; Luchian, T. Electroosmotic trap against the electrophoretic force near a protein nanopore reveals peptide dynamics during capture and translocation. *ACS Appl. Mater. Interfaces* **2016**, *8*, 13166–13179.
(12) Huang, G.; Willems, K.; Soskine, M.; Wloka, C.; Maglia, G. Electro-osmotic capture and ionic discrimination of peptide and protein biomarkers with FraC nanopores. *Nat. Commun.* **2017**, *8*, 935.
(13) Boukhet, M.; Piguet, F.; Ouldali, H.; Pastoriza-Gallego, M.; Pelta, J.; Oukhaled, A. Probing driving forces in aerolysin and α-hemolysin biological nanopores: electrophoresis versus electroosmosis. *Nanoscale* **2016**, *8*, 18352–18359.
(14) Baldelli, M.; Di Muccio, G.; Sauciuc, A.; Morozzo della Rocca, B.; Viola, F.; Balme, S.; Bonini, A.; Maglia, G.; Chinappi, M. Controlling Electroosmosis in Nanopores Without Altering the Nanopore Sensing Region. *Adv. Mater.* **2024**, *36*, 2401761.
(15) Mehrafrooz, B.; Yu, L.; Pandey, L.; Siwy, Z. S.; Wanunu, M.; Aksimentiev, A. Electro-osmotic flow generation via a sticky ion action. *ACS Nano* **2024**, *18*, 17521–17533.
(16) Sauciuc, A.; Morozzo della Rocca, B.; Tadema, M. J.; Chinappi, M.; Maglia, G. Translocation of linearized full-length proteins through an engineered nanopore under opposing electrophoretic force. *Nat. Biotechnol.* **2024**, *42*, 1275–1281.
(17) Meyer, N.; Ratinho, L.; Greive, S. J.; Bacri, L.; Thiebot, B.; Morozzo della Rocca, B.; Chinappi, M.; Pelta, J.; Cressiot, B. Discrimination of Oxytocin, a Behavioral Neuropeptide Hormone, and Its Structural Variants by Nanopore. *ACS Nano* **2025**, *19*, 28690–28701.
(18) Jiang, J.; Li, M.-Y.; Wu, X.-Y.; Ying, Y.-L.; Han, H.-X.; Long, Y.-T. Protein nanopore reveals the renin–angiotensin system crosstalk with single-amino-acid resolution. *Nat. Chem.* **2023**, *15*, 578–586.
(19) Li, M.-Y.; Jiang, J.; Li, J.-G.; Niu, H.; Ying, Y.-L.; Tian, R.; Long, Y.-T. Nanopore approaches for single-molecule temporal omics: promises and challenges. *Nat. Methods* **2025**, *22*, 241–253.
(20) Gubbiotti, A.; Baldelli, M.; Di Muccio, G.; Malgaretti, P.; Marbach, S.; Chinappi, M. Electroosmosis in nanopores: computational methods and technological applications. *Adv. Phys.: X* **2022**, *7*, 2036638.
(21) Bonome, E. L.; Cecconi, F.; Chinappi, M. Electroosmotic flow through an α-hemolysin nanopore. *Microfluid. Nanofluid.* **2017**, *21*, 96.
(22) Aksimentiev, A.; Schulten, K. Imaging α-hemolysin with molecular dynamics: ionic conductance, osmotic permeability, and the electrostatic potential map. *Biophys. J.* **2005**, *88*, 3745–3761.
(23) Piguet, F.; Discala, F.; Breton, M.-F.; Pelta, J.; Bacri, L.; Oukhaled, A. Electroosmosis through α-hemolysin that depends on alkali cation type. *J. Phys. Chem. Lett.* **2014**, *5*, 4362–4367.
(24) Bhattacharya, S.; Muzard, J.; Payet, L.; Mathé, J.; Bockelmann, U.; Aksimentiev, A.; Viasnoff, V. Rectification of the current in α-hemolysin pore depends on the cation type: the alkali series probed by molecular dynamics simulations and experiments. *J. Phys. Chem. C* **2011**, *115*, 4255–4264.
(25) Zhang, M.; Tang, C.; Wang, Z.; Chen, S.; Zhang, D.; Li, K.; Sun, K.; Zhao, C.; Wang, Y.; Xu, M., et al. Real-time detection of 20 amino acids and discrimination of pathologically relevant peptides with functionalized nanopore. *Nat. Methods* **2024**, *21*, 609–618.
(26) Wang, K.; Zhang, S.; Zhou, X.; Yang, X.; Li, X.; Wang, Y.; Fan, P.; Xiao, Y.; Sun, W.; Zhang, P., et al. Unambiguous discrimination of all 20 proteinogenic amino acids and their modifications by nanopore. *Nat. Methods* **2024**, *21*, 92–101.
(27) Yan, S.; Wang, L.; Du, X.; Zhang, S.; Wang, S.; Cao, J.; Zhang, J.; Jia, W.; Wang, Y.; Zhang, P., et al. Rapid and multiplex preparation of engineered Mycobacterium smegmatis porin A (MspA) nanopores for single molecule sensing and sequencing. *Chem. Sci.* **2021**, *12*, 9339–9346.
(28) Liu, Y.; Wang, K.; Wang, Y.; Wang, L.; Yan, S.; Du, X.; Zhang, P.; Chen, H.-Y.; Huang, S. Machine learning assisted simultaneous structural profiling of differently charged proteins in a Mycobacterium smegmatis porin A (MspA) electroosmotic trap. *J. Am. Chem. Soc.* **2022**, *144*, 757–768.
(29) Wang, Y.; Guan, X.; Zhang, S.; Liu, Y.; Wang, S.; Fan, P.; Du, X.; Yan, S.; Zhang, P.; Chen, H.-Y., et al. Structural-profiling of low molecular weight RNAs by nanopore trapping/translocation using Mycobacterium smegmatis porin A. *Nat. Commun.* **2021**, *12*, 3368.
(30) Braha, O.; Walker, B.; Cheley, S.; Kasianowicz, J. J.; Song, L.; Gouaux, J. E.; Bayley, H. Designed protein pores as components for biosensors. *Chem. Biol.* **1997**, *4*, 497–505.
(31) Bhamidimarri, S. P.; Prajapati, J. D.; van den Berg, B.; Winterhalter, M.; Kleinekathöfer, U. Role of electroosmosis in the permeation of neutral molecules: CymA and cyclodextrin as an example. *Biophys. J.* **2016**, *110*, 600–611.
(32) Zhang, Y.; Liu, L.; Sha, J.; Ni, Z.; Yi, H.; Chen, Y. Nanopore detection of DNA molecules in magnesium chloride solutions. *Nanoscale Res. Lett.* **2013**, *8*, 245.
(33) Roodhuizen, J. A.; Hendrikx, P. J.; Hilbers, P. A.; de Greef, T. F.; Markvoort, A. J. Counterion-dependent mechanisms of DNA origami nanostructure stabilization revealed by atomistic molecular simulation. *ACS Nano* **2019**, *13*, 10798–10809.
(34) Dutt, S.; Lai, L. B.; Mehta, R.; Karawdeniya, B. I.; Bandara, Y. N. D.; Clulow, A. J.; Glatt, S.; Gopalan, V.; Kluth, P. Solid-state nanopore sensing reveals conformational changes induced by a mutation in a neuron-specific tRNAArg. *Nucleic Acids Res.* **2026**, *54*, gkaf1411.
(35) Li, M.-Y.; Niu, H.; Jiang, J.; Wu, X.-Y.; Ying, Y.-L.; Long, Y.-T. Real-time recording the dynamic catalytic heterogeneity of enzymatic reactions using a nanopore. *J. Am. Chem. Soc.* **2025**, *147*, 17121–17131.
(36) Manrao, E. A.; Derrington, I. M.; Laszlo, A. H.; Langford, K. W.; Hopper, M. K.; Gillgren, N.; Pavlenok, M.; Niederweis, M.; Gundlach, J. H. Reading DNA at single-nucleotide resolution with a mutant MspA nanopore and phi29 DNA polymerase. *Nat. Biotechnol.* **2012**, *30*, 349.
(37) Fuller, C. W.; Kumar, S.; Porel, M.; Chien, M.; Bibillo, A.; Stranges, P. B.; Dorwart, M.; Tao, C.; Li, Z.; Guo, W., et al. Real-time single-molecule electronic DNA sequencing by synthesis using polymer-tagged nucleotides on a nanopore array. *Proc. Natl. Acad. Sci. U. S. A.* **2016**, *113*, 5233–5238.
(38) Craig, J. M.; Laszlo, A. H.; Nova, I. C.; Brinkerhoff, H.; Noakes, M. T.; Baker, K. S.; Bowman, J. L.; Higinbotham, H. R.; Mount, J. W.; Gundlach, J. H. Determining the effects of DNA sequence on Hel308 helicase translocation along single-stranded DNA using nanopore tweezers. *Nucleic Acids Res.* **2019**, *47*, 2506–2513.
(39) Brinkerhoff, H.; Kang, A. S.; Liu, J.; Aksimentiev, A.; Dekker, C. Multiple rereads of single proteins at single–amino acid resolution using nanopores. *Science* **2021**, *374*, 1509–1513.
(40) Yan, S.; Zhang, J.; Wang, Y.; Guo, W.; Zhang, S.; Liu, Y.; Cao, J.; Wang, Y.; Wang, L.; Ma, F., et al. Single molecule ratcheting motion of peptides in a Mycobacterium smegmatis porin A (MspA) nanopore. *Nano Lett.* **2021**, *21*, 6703–6710.
(41) Chen, Z.; Wang, Z.; Xu, Y.; Zhang, X.; Tian, B.; Bai, J. Controlled movement of ssDNA conjugated peptide through Mycobacterium smegmatis porin A (MspA) nanopore by a helicase motor for peptide sequencing application. *Chem. Sci.* **2021**, *12*, 15750–15756.
(42) Wang, Y.; Fan, P.; Zhang, S.; Wang, L.; Li, X.; Jia, W.; Liu, Y.; Wang, K.; Du, X.; Zhang, P., et al. Discrimination of ribonucleoside mono-, di-, and triphosphates using an engineered nanopore. *ACS Nano* **2022**, *16*, 21356–21365.
(43) Butler, T. Z.; Pavlenok, M.; Derrington, I. M.; Niederweis, M.; Gundlach, J. H. Single-molecule DNA detection with an engineered MspA protein nanopore. *Proc. Natl. Acad. Sci. U. S. A.* **2008**, *105*, 20647–20652.
(44) Saharia, J.; Bandara, Y. N. D.; Karawdeniya, B. I.; Hammond, C.; Alexandrakis, G.; Kim, M. J. Modulation of electrophoresis, electroosmosis and diffusion for electrical transport of proteins through a solid-state nanopore. *RSC Adv.* **2021**, *11*, 24398–24409.
(45) Gargano, S.; Iacoviello, D. F.; Iacovelli, F.; Morozzo della Rocca, B.; Chinappi, M. Comparison among Amber-ff14SB, Amber-ff19SB,

and CHARMM36 Force Fields for Ionic and Electroosmotic Flows in Biological Nanopores. *J. Chem. Theory Comput.* **2025**, *21*, 11772.
(46) Reccia, M.; Quilli, F.; Willems, K.; Della Rocca, B. M.; Raimondo, D.; Chinappi, M. Bioinformatic and computational biophysics tools for nanopore engineering: a review from standard approaches to machine learning advancements. *J. Nanobiotechnol.* **2026**, *24*, 343.
(47) Di Muccio, G.; Gargano, S.; Iacoviello, D. F.; della Rocca, B. M.; Chinappi, M. Validity of approximated expressions for electro-osmotic flow in nanopores evaluated by continuum electrohydrodynamics and atomistic simulations. *Flow* **2025**, *5*, E28.
(48) Modi, N.; Winterhalter, M.; Kleinekathoefer, U. Computational modeling of ion transport through nanopores. *Nanoscale* **2012**, *4*, 6166–6180.
(49) Phillips, J. C.; Braun, R.; Wang, W.; Gumbart, J.; Tajkhorshid, E.; Villa, E.; Chipot, C.; Skeel, R. D.; Kale, L.; Schulten, K. Scalable molecular dynamics with NAMD. *J. Comput. Chem.* **2005**, *26*, 1781–1802.
(50) Di Muccio, G.; Morozzo della Rocca, B.; Chinappi, M. Geometrically induced selectivity and unidirectional electroosmosis in uncharged nanopores. *ACS Nano* **2022**, *16*, 8716–8728.
(51) Klauda, J. B.; Venable, R. M.; Freites, J. A.; O'Connor, J. W.; Tobias, D. J.; Mondragon-Ramirez, C.; Vorobyov, I.; MacKerell, A. D.; Pastor, R. W. Update of the CHARMM all-atom additive force field for lipids: validation on six lipid types. *J. Phys. Chem. B* **2010**, *114*, 7830–7843.
(52) Yoo, J.; Aksimentiev, A. Improved parametrization of Li+, Na+, K+, and Mg2+ ions for all-atom molecular dynamics simulations of nucleic acid systems. *J. Phys. Chem. Lett.* **2012**, *3*, 45–50.
(53) Essmann, U.; Perera, L.; Berkowitz, M. L.; Darden, T.; Lee, H.; Pedersen, L. G. A smooth particle mesh Ewald method. *J. Chem. Phys.* **1995**, *103*, 8577–8593.
(54) Martyna, G. J.; Tobias, D. J.; Klein, M. L. Constant pressure molecular dynamics algorithms. *J. Chem. Phys.* **1994**, *101*, 4177–4189.
(55) Case, D. A.; Aktulga, H. M.; Belfon, K.; Cerutti, D. S.; Cisneros, G. A.; Cruzeiro, V. W. D.; Forouzesh, N.; Giese, T. J.; Götz, A. W.; Gohlke, H., et al. AmberTools. *J. Chem. Inform. Model.* **2023**, *63*, 6183–6191.
(56) Faller, M.; Niederweis, M.; Schulz, G. E. The structure of a mycobacterial outer-membrane channel. *Science* **2004**, *303*, 1189–1192.
(57) Lomize, M. A.; Lomize, A. L.; Pogozheva, I. D.; Mosberg, H. I. OPM: orientations of proteins in membranes database. *Bioinformatics* **2006**, *22*, 623–625.
(58) Humphrey, W.; Dalke, A.; Schulten, K., et al. VMD: visual molecular dynamics. *J. Mol. Graph.* **1996**, *14*, 33–38.
(59) Maier, J. A.; Martinez, C.; Kasavajhala, K.; Wickstrom, L.; Hauser, K. E.; Simmerling, C. ff14SB: improving the accuracy of protein side chain and backbone parameters from ff99SB. *J. Chem. Theory Comput.* **2015**, *11*, 3696–3713.
(60) Tian, C.; Kasavajhala, K.; Belfon, K. A.; Raguette, L.; Huang, H.; Migues, A. N.; Bickel, J.; Wang, Y.; Pincay, J.; Wu, Q., et al. ff19SB: amino-acid-specific protein backbone parameters trained against quantum mechanics energy surfaces in solution. *J. Chem. Theory Comput.* **2019**, *16*, 528–552.
(61) Jorgensen, W. L.; Chandrasekhar, J.; Madura, J. D.; Impey, R. W.; Klein, M. L. Comparison of simple potential functions for simulating liquid water. *J. Chem. Phys.* **1983**, *79*, 926–935.
(62) Izadi, S.; Anandakrishnan, R.; Onufriev, A. V. Building water models: a different approach. *J. Phys. Chem. Lett.* **2014**, *5*, 3863–3871.
(63) Won, Y. Force field for monovalent, divalent, and trivalent cations developed under the solvent boundary potential. *J. Phys. Chem. A* **2012**, *116*, 11763–11767.
(64) Sauciuc, A.; Whittaker, J.; Tadema, M.; Tych, K.; Guskov, A.; Maglia, G. Blobs form during the single-file transport of proteins across nanopores. *Proc. Natl. Acad. Sci. U. S. A.* **2024**, *121*, e2405018121.
(65) Maglia, G.; Heron, A. J.; Stoddart, D.; Japrung, D.; Bayley, H. *Methods in enzymology*; Elsevier, **2010**; Vol *475*; pp 591–623.
(66) Vreeker, E.; Grünewald, F.; van der Heide, N. J.; Bonini, A.; Marrink, S. J.; Tych, K.; Maglia, G. Nanopore-Functionalized Hybrid Lipid-Block Copolymer Membranes Allow Efficient Single-Molecule Sampling and Stable Sensing of Human Serum. *Adv. Mater.* **2025**, *37*, 2418462.

https://doi.org/10.1021/acsami.6c06920
ACS Appl. Mater. Interfaces XXXX, XXX, XXX–XXX